Nigerian Journal of Environmental Sciences and Technology
(NIJEST)
www.nijest.com
ISSN (Print): 2734-259X | ISSN (electronic): 2734-2603
Vol 9, No. 2 October 2025, pp 181 - 195

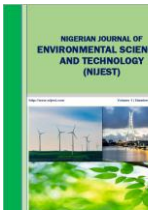

Effects of Limestone Mining Activities on Land Use and Land Cover Change Around Dangote Cement Factory, Gboko, Benue State

Dzever L.F.[1], Shomkegh S.A. [1,2] and Ugbaa M.S. [1,3]
[1]Department of Environmental Sustainability, Joseph Sarwuan Tarka University, Makudi Benue State Nigeria
[2]Department of Forest Production and Products, Joseph Sarwuan Tarka University, Makudi Benue State Nigeria
[3]Department of Plant Breeding and Seed Science, Joseph Sarwuan Tarka University, Makudi Benue State Nigeria

*Corresponding author: fanen5925@gmail.com

https://doi.org/10.36263/nijest.2025.02.64

ABSTRACT

The understanding of long-term land use and land cover (LULC) dynamics is essential for effective environmental management and sustainable urban planning. This study investigates spatio-temporal LULC changes within the study area over a 38-year period using multi-temporal Landsat satellite imagery acquired for 1986, 2013, 2019, and 2024. Landsat 5 TM, Landsat 7 ETM+, Landsat 8 OLI, and Landsat 9 OLI-2 surface reflectance datasets were processed within the Google Earth Engine platform. Image pre-processing involved cloud and shadow masking, temporal filtering, and generation of median composites to ensure radiometric consistency and minimize noise. To improve class separability, key spectral indices, Normalized Difference Vegetation Index (NDVI), Normalized Difference Built-up Index (NDBI), Modified Normalized Difference Water Index (MNDWI), and Bare Soil Index (BSI), were derived and integrated with Landsat spectral bands. Land cover classification was performed using the Random Forest machine learning algorithm, with four major classes identified: water, built-up areas, vegetation, and bare soil. Classification accuracy was evaluated using independent validation samples and standard accuracy metrics. The results indicate high classification performance, with overall accuracies of 93.33% (κ = 0.89) for 1986, 85.00% (κ = 0.79) for 2013, 87.50% (κ = 0.83) for 2019, and 82.76% (κ = 0.76) for 2024. Change detection analysis revealed substantial expansion of built-up areas, a decline and subsequent recovery of vegetation cover, increasing water bodies, and dynamic transitions in bare soil areas. These findings demonstrate the effectiveness of integrating spectral indices and machine learning for long-term LULC monitoring and provide valuable insights for land management and urban development planning.

Keywords: Land Use/Land Cover Change; Remote Sensing; Random Forest Classification; Google Earth Engine; Landsat Imagery

1.0. Introduction

Globally, many countries are experiencing rapid and persistent changes in land use and land cover (LULC), driven largely by the complex interactions between human activities and natural environmental processes. These changes have become one of the most significant indicators of anthropogenic pressure on the Earth's surface and are increasingly recognized as a critical component of global environmental change. Understanding the nature, magnitude, drivers, and consequences of LULC change is therefore essential for informed decision-making and sustainable development planning (Gondwe et al., 2021).

Land cover refers to the observable physical and biophysical characteristics of the Earth's surface, including vegetation, water bodies, soil, and built-up features, whereas land use describes how humans utilize land for social, economic, political, or cultural purposes (Verburg et al., 2015). Land

change occurs when these characteristics are modified, either through conversion from one land cover or land use type to another or through intensification of existing land use practices. Such changes are predominantly induced by anthropogenic activities, although natural factors such as climate variability and geomorphological processes also contribute to land surface transformations (Dadson, 2016; Liping et al., 2018).

Human-driven activities including agriculture, mining, overgrazing, residential and industrial expansion, and infrastructure development have accelerated land use transitions, particularly in rapidly developing regions. Population growth and increasing demand for food, energy, and raw materials further intensify the exploitation of natural resources, often leading to environmental degradation (Liping et al., 2018). These transformations have far-reaching environmental consequences, including deforestation, biodiversity loss, soil degradation, disruption of hydrological systems, food insecurity, and increased emissions of carbon dioxide and other greenhouse gases, thereby exacerbating global climate change (Cobbinah et al., 2015; Clerici et al., 2019; Hu et al., 2019).

Urbanization remains a dominant driver of LULC change worldwide. According to the United Nations, more than 50% of the global population resided in urban areas as of 2014, a proportion that continues to rise. This rapid urban growth inevitably results in the conversion of natural and agricultural lands into built-up areas, altering ecosystem functions and landscape structure. Concurrently, economic development increases pressure on land resources as societies seek to meet growing energy and food demands (Abass et al., 2018).

Comprehensive knowledge of LULC dynamics is therefore indispensable for stakeholders such as urban planners, environmental protection agencies, and local authorities. Accurate and timely information on land use and land cover changes supports effective natural resource management, environmental monitoring, and spatial planning, while also enabling the assessment and prediction of human-induced environmental changes. Such insights are crucial for balancing development needs with environmental conservation and for achieving sustainable development goals that safeguard resources for future generations (Kumasi et al., 2010; Kamwi et al., 2015; Gondwe et al., 2021).

2.0. Methodology

2.1. Study Area

The study was conducted in Mbatyu Council Ward, located in Mbayion District, Gboko Local Government Area (LGA), Benue State, Nigeria, where the Dangote Cement Factory is located as indicated by Figure 1. The area is geographically positioned between latitudes 7°24'N and 7°25'N and longitudes 8°57'E and 8°59'E of the Greenwich Meridian. Gboko is a major center of limestone mining and is home to Dangote Cement, one of the largest cement producers in Nigeria.

The region experiences a tropical climate characterized by two main seasons: the wet season (April to October) and the dry season (November to March). The average annual rainfall ranges between 1200mm and 1800mm, with higher precipitation during the wet season, while the dry season is marked by the harmattan winds, which lower humidity levels significantly.

The natural vegetation consists predominantly of savannah grassland interspersed with patches of woodland, but large portions of this have been cleared due to farming and industrial activities, particularly limestone mining. Geologically, the area lies within the Benue Trough, a rich sedimentary basin with large deposits of limestone, which is primarily exploited for cement production. Mbatyu is surrounded by other wards like Mbatan, Mba Avarakaa, Mbatser, Ukpekpe, and Gboko Central, which are integral parts of the socio-economic and land use context of the region.

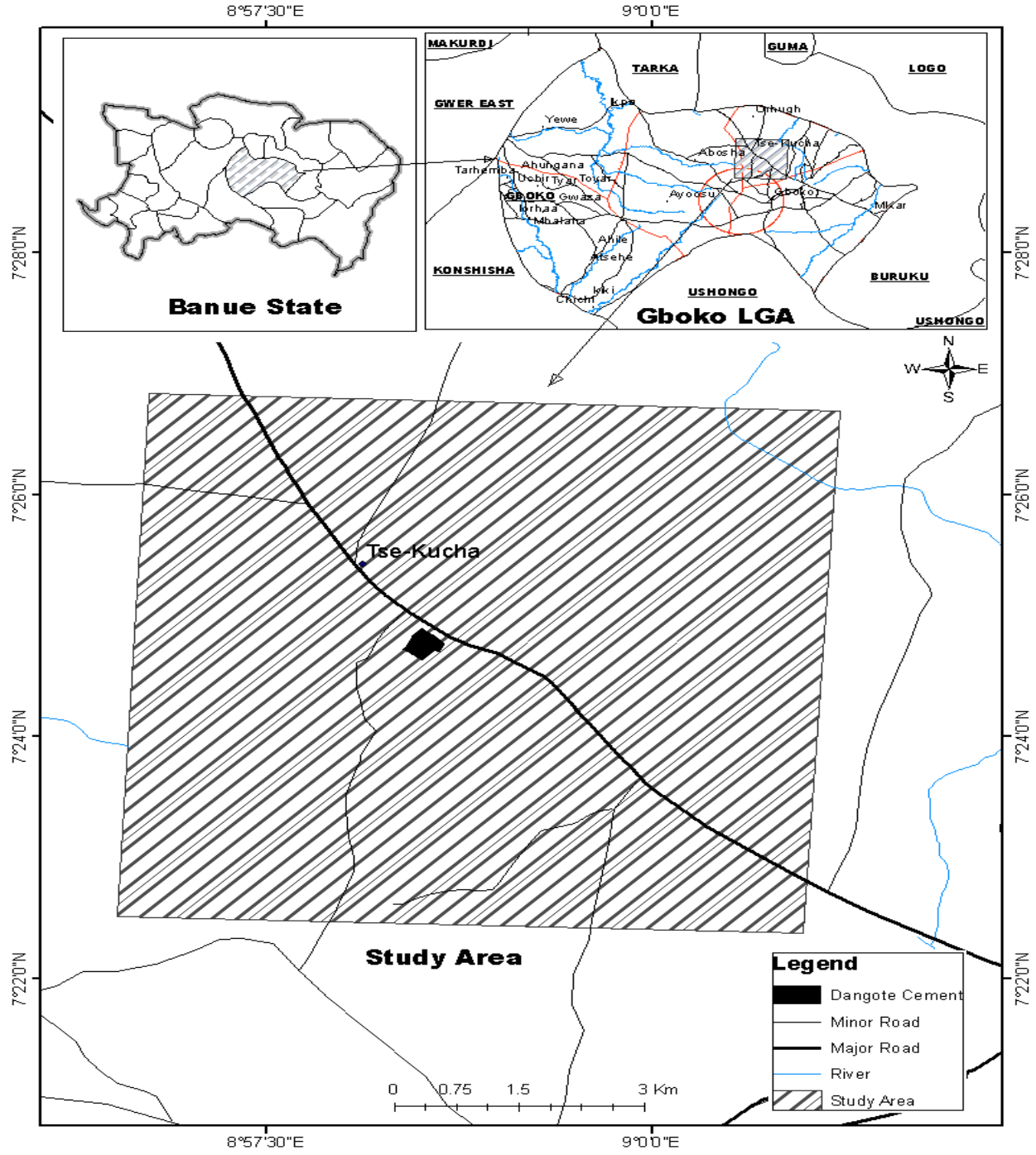

Figure 1: Map of Benue State showing the Study areas

2.2 Data Sources and Image Pre-processing

Multi-temporal satellite imagery was employed to investigate land use and land cover (LULC) dynamics within the study area for four representative epochs: 1986, 2013, 2019, and 2024. Landsat imagery was selected due to its long temporal coverage, consistent spatial resolution, and proven suitability for long-term environmental monitoring and change detection studies.

Landsat 5 Thematic Mapper (TM) imagery was used for 1986, Landsat 7 Enhanced Thematic Mapper Plus (ETM+) for 2013, Landsat 8 Operational Land Imager (OLI) for 2019, and Landsat 9 Operational Land Imager–2 (OLI-2) for 2024. All datasets were sourced from the United States Geological Survey (USGS) Landsat Collection 2 Level-2 Surface Reflectance archive and processed within the Google Earth Engine (GEE) cloud-computing environment. The Level-2 products were selected because they are radiometrically calibrated and atmospherically corrected, thereby ensuring consistency and reliability for quantitative analysis across multiple time periods.

To reduce the influence of cloud contamination and atmospheric artefacts, image collections for each year were filtered based on acquisition date and cloud cover percentage. Cloud and cloud shadow pixels were identified and removed using the quality assurance (QA) bands accompanying the surface reflectance products. For each epoch, a median composite image was generated from the filtered image collection to represent typical surface conditions while minimizing residual noise, outliers, and seasonal variability.

All composite images were spatially clipped to the study area boundary to maintain uniform spatial extent across all years. The native Landsat spatial resolution of 30 m was preserved throughout the analysis, enabling direct inter-annual comparison of LULC patterns. Although Sentinel-2 surface reflectance imagery was available for 2024, it was not incorporated into the classification process. Instead, it was used as a high-resolution reference dataset to support training sample selection and improve visual interpretation of land cover classes.

2.3 Spectral Index Derivation

To enhance class separability and improve classification performance, a set of spectral indices was derived from the Landsat surface reflectance imagery for each study year. These indices were selected based on their established effectiveness in discriminating vegetation, built-up areas, water bodies, and bare soil, which constitute the dominant land cover types within the study area. Prior to index computation, Landsat Level-2 surface reflectance bands were radiometrically scaled using the standard scale factors provided by the data producer to ensure physical consistency of reflectance values.

2.4 Normalized Difference Vegetation Index (NDVI)

Vegetation characteristics were quantified using the Normalized Difference Vegetation Index (NDVI), which exploits the contrast between strong near-infrared reflectance and red-band absorption by healthy vegetation. NDVI is defined as shown by equation 1:

$$NDVI = \frac{NIR - \mathrm{Re}\,d}{NIR + \mathrm{Re}\,d} \quad (1)$$

For Landsat imagery, the near-infrared and red bands correspond to Band 5 (SR_B5) and Band 4 (SR_B4), respectively. Higher NDVI values indicate dense and healthy vegetation, whereas low or negative values are associated with non-vegetated surfaces such as built-up areas, bare soil, and water bodies.

2.5 Normalized Difference Built-up Index (NDBI)

Built-up and impervious surfaces were enhanced using the Normalized Difference Built-up Index (NDBI), which leverages the higher reflectance of urban materials in the shortwave infrared (SWIR) region relative to the near-infrared region. The NDBI is expressed as shown in equation 2:

$$NDBI = \frac{SWIR - NIR}{SWIR + NIR} \quad (2)$$

In this study, SWIR corresponds to Band 6 (SR_B6) and NIR to Band 5 (SR_B5). Positive NDBI values generally indicate built-up areas, while negative values are characteristic of vegetated and water-covered surfaces.

2.6 Modified Normalized Difference Water Index (MNDWI)

Surface water features were delineated using the Modified Normalized Difference Water Index (MNDWI), which improves water detection by suppressing noise from vegetation and built-up areas. The index is computed using equation 3:

$$MNDWI = \frac{Green - SWIR}{Green + SWIR} \quad (3)$$

For Landsat imagery, the green band corresponds to Band 3 (SR_B3), while the SWIR band corresponds to Band 6 (SR_B6). Water bodies typically exhibit positive MNDWI values, whereas non-water features yield negative responses.

2.7 Bare Soil Index (BSI)

Exposed soil and sparsely vegetated surfaces were identified using the Bare Soil Index (BSI), which integrates information from the blue, red, near-infrared, and shortwave infrared bands. The BSI is defined using equation 4:

$$NDBI = \frac{(SWIR + \mathrm{Re}\,d) - (NIR + Blue)}{(SWIR + \mathrm{Re}\,d) + (NIR + Blue)} \quad (4)$$

In this formulation, the blue, red, near-infrared, and SWIR bands correspond to SR_B2, SR_B4, SR_B5, and SR_B6, respectively. Higher BSI values indicate bare or exposed soil surfaces, while lower values correspond to vegetated or water-covered areas.

2.8 Integration of Spectral Indices

The computed NDVI, NDBI, MNDWI, and BSI layers were appended to the original Landsat spectral bands and jointly used during training sample selection and image classification. The integration of these indices enhanced spectral discrimination among land cover classes by capturing their distinct biophysical characteristics, thereby improving classification robustness and accuracy.

2.9 Training Sample Selection and Random Forest Classification

Land use and land cover classification was performed using the Random Forest (RF) machine learning algorithm implemented within the Google Earth Engine platform. RF was selected due to its high classification accuracy, robustness to noise, and ability to handle multicollinearity among input variables. Four major LULC classes were defined: water, built-up areas, vegetation, and bare soil.

Training samples for each class were carefully selected through a combination of spectral index thresholding and visual interpretation of high-resolution imagery. Sentinel-2 imagery was employed as an auxiliary reference for more accurate sample identification, particularly for the 2019 and 2024 datasets. All samples were merged into a single feature collection and randomly partitioned into training and testing subsets, with approximately 70% of the samples used for model training and the remaining 30% reserved for independent validation.

The RF classifier was trained using Landsat optical bands (SR_B1 to SR_B6) together with the derived spectral indices (NDVI, NDBI, MNDWI, and BSI) as input features. The number of decision trees was varied during model development, and classifier performance was evaluated iteratively to determine optimal model parameters. Once trained, the classifier was applied to the full spatial extent of the study area to generate LULC maps for each reference year.

2.10 Accuracy Assessment

Classification accuracy was assessed using the independent testing subset of samples. An error (confusion) matrix was generated for each classified map, from which standard accuracy metrics were derived. Overall accuracy (OA) was computed as the proportion of correctly classified pixels relative to the total number of validation pixels, while the Kappa coefficient (κ) was used to quantify the level of agreement between the classified maps and reference data beyond chance. Producer's accuracy (PA), which reflects omission errors, was calculated as the ratio of correctly classified pixels in a given class to the total number of reference pixels for that class using equation 5:

$$PA = \frac{Correctly\ classified\ \ pixels\ in\ a\ class}{Total\ \ reference\ \ pixels\ in\ that\ class} \quad (5)$$

In the same manner, the User's accuracy (UA) which indicates commission errors, was computed as the ratio of correctly classified pixels in a class to the total number of pixels classified into that class was calculated using equation 6:

$$UA = \frac{Correctly\ classified\ \ pixels\ in\ a\ class}{Total\ \ reference\ \ pixels\ as\ that\ class} \quad (6)$$

3.0 Results and Discussion

3.1 Classification Accuracy and Model Performance

Table 1: The classification accuracy for each year

Year	Samples (n)	Training	Testing	Overall Accuracy	Kappa
1986	60	45	15	93.33%	0.89
2013	87	67	20	85.00%	0.79
2019	146	106	40	87.50%	0.83
2024	89	60	29	82.76%	0.76

The Random Forest (RF) classifier presented in Table 1 demonstrated good performance in mapping land use and land cover (LULC) across all four study epochs (1986, 2013, 2019, and 2024). Overall classification accuracies ranged from 82.76% to 93.33%, with corresponding Kappa coefficients between 0.76 and 0.89, indicating substantial to almost perfect agreement between classified outputs and reference data. The highest accuracy was recorded for 1986 (OA = 93.33%, $\kappa = 0.89$), while the lowest occurred in 2024 (OA = 82.76%, $\kappa = 0.76$). These values are consistent with previous LULC studies employing Random Forest classifiers, which commonly report overall accuracies above 80% when multi-spectral Landsat data and spectral indices are integrated (Kumasi et al., 2010; Kamwi et al., 2015; Gondwe et al., 2021).

The marginal reduction in classification accuracy observed in the more recent datasets can be attributed to increasing landscape complexity and spectral heterogeneity caused by rapid urban expansion and mixed land cover patterns. Similar declines in classification accuracy for recent periods have been reported in urbanizing environments, where spectral confusion between built-up areas, bare soil, and sparsely vegetated surfaces is more pronounced (Clerici et al., 2019; Hu et al., 2019). Nevertheless, the achieved accuracy levels confirm the suitability of the RF algorithm and the derived spectral indices for reliable multi-temporal LULC mapping.

3.2 Spatio-Temporal Patterns of Land Use and Land Cover Change

Figure 2 to Figure 4 represent the spatial distribution and temporal evolution of LULC classes reveal significant land transformation over the 38-year study period. In 1986, the landscape was dominated by vegetation (4.19 km²) and bare soil (4.65 km²), with built-up areas occupying a relatively small proportion (0.33 km²) and no detectable surface water. This land cover configuration is typical of less urbanized landscapes, as reported in earlier studies across developing regions (Dadson, 2016; Liping et al., 2018).

By 2013, built-up areas expanded markedly to 1.34 km², reflecting intensified urbanization and infrastructural development. This expansion coincided with a substantial reduction in vegetation cover to 2.37 km² and an increase in bare soil to 5.28 km², suggesting widespread land clearing and transitional land states associated with construction activities. Comparable patterns of vegetation loss and bare land expansion during early phases of urban growth have been widely documented in rapidly developing cities (Cobbinah et al., 2015; Abass et al., 2018).

Between 2013 and 2019, built-up land continued to increase, reaching 1.88 km², while vegetation cover exhibited partial recovery to 3.36 km². This trend persisted into 2024, with built-up areas expanding further to 2.01 km² and vegetation increasing to 3.74 km². The observed vegetation recovery may be attributed to land management practices, re-vegetation initiatives, or natural regeneration following earlier disturbances. Similar post-urbanization vegetation recovery trends have been reported in studies where urban expansion stabilizes or where green infrastructure policies are implemented (Kamwi et al., 2015; Clerici et al., 2019).

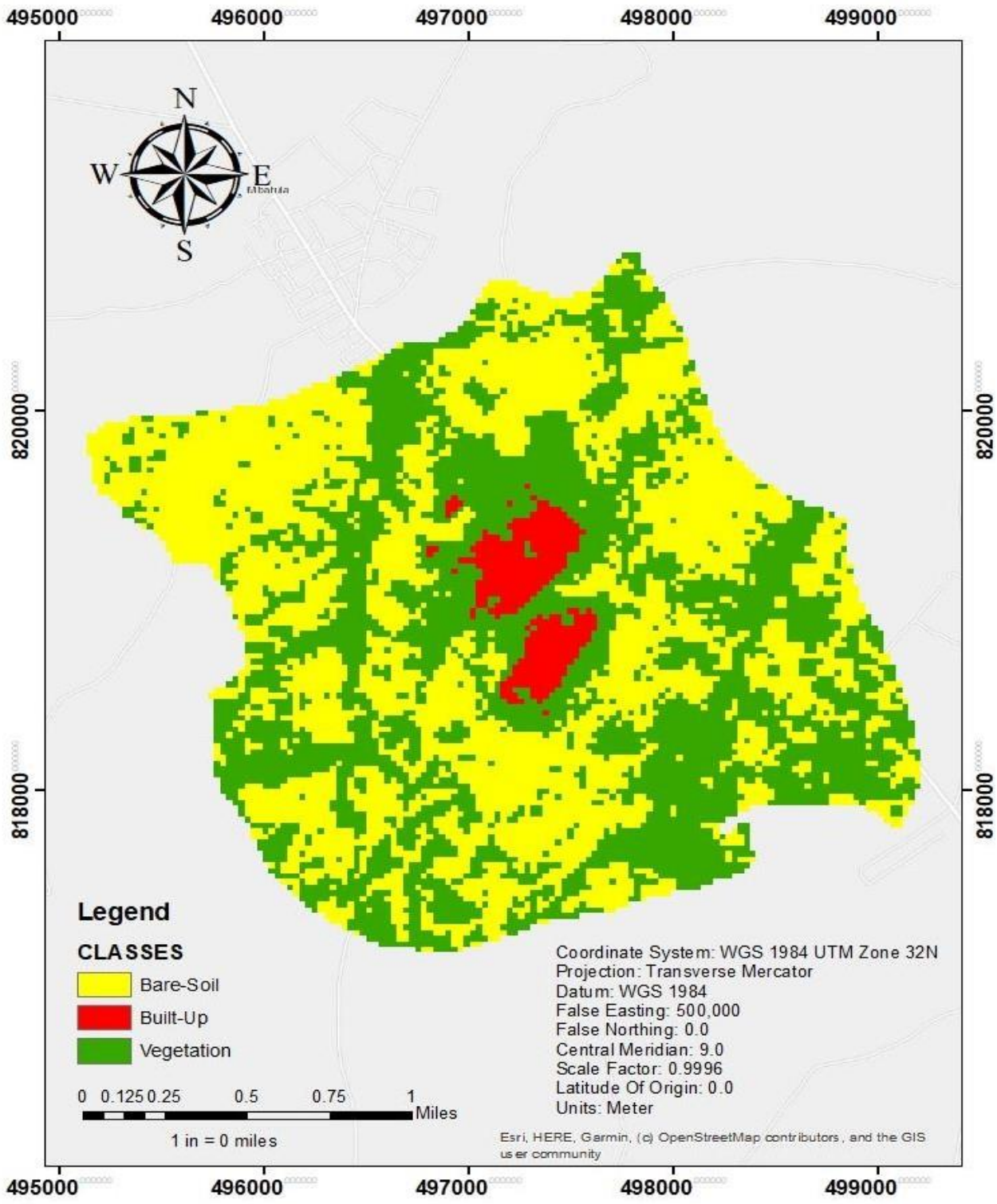

Figure 2: LULC map for 1986

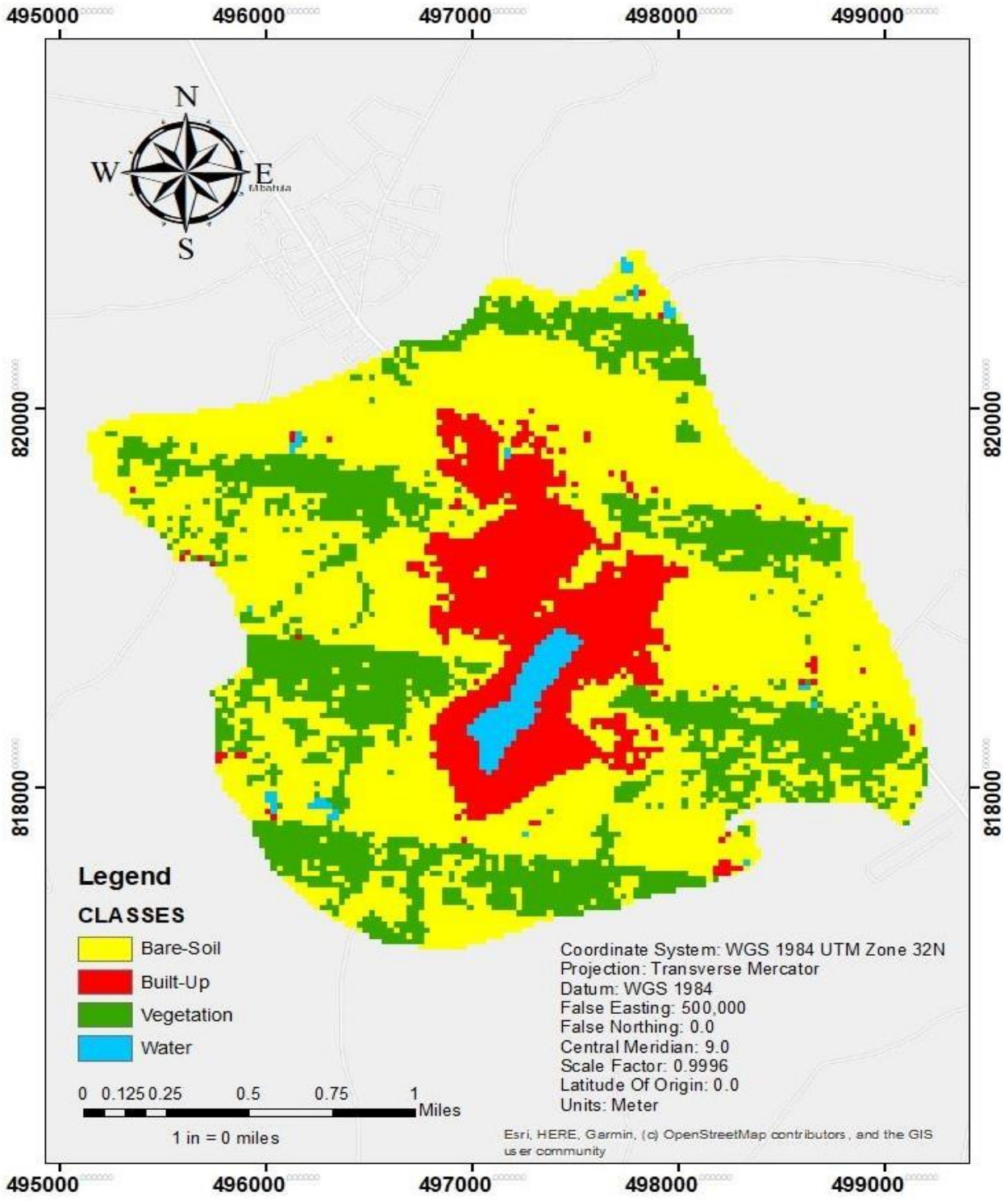

Figure 4.2: LULC map for 2013

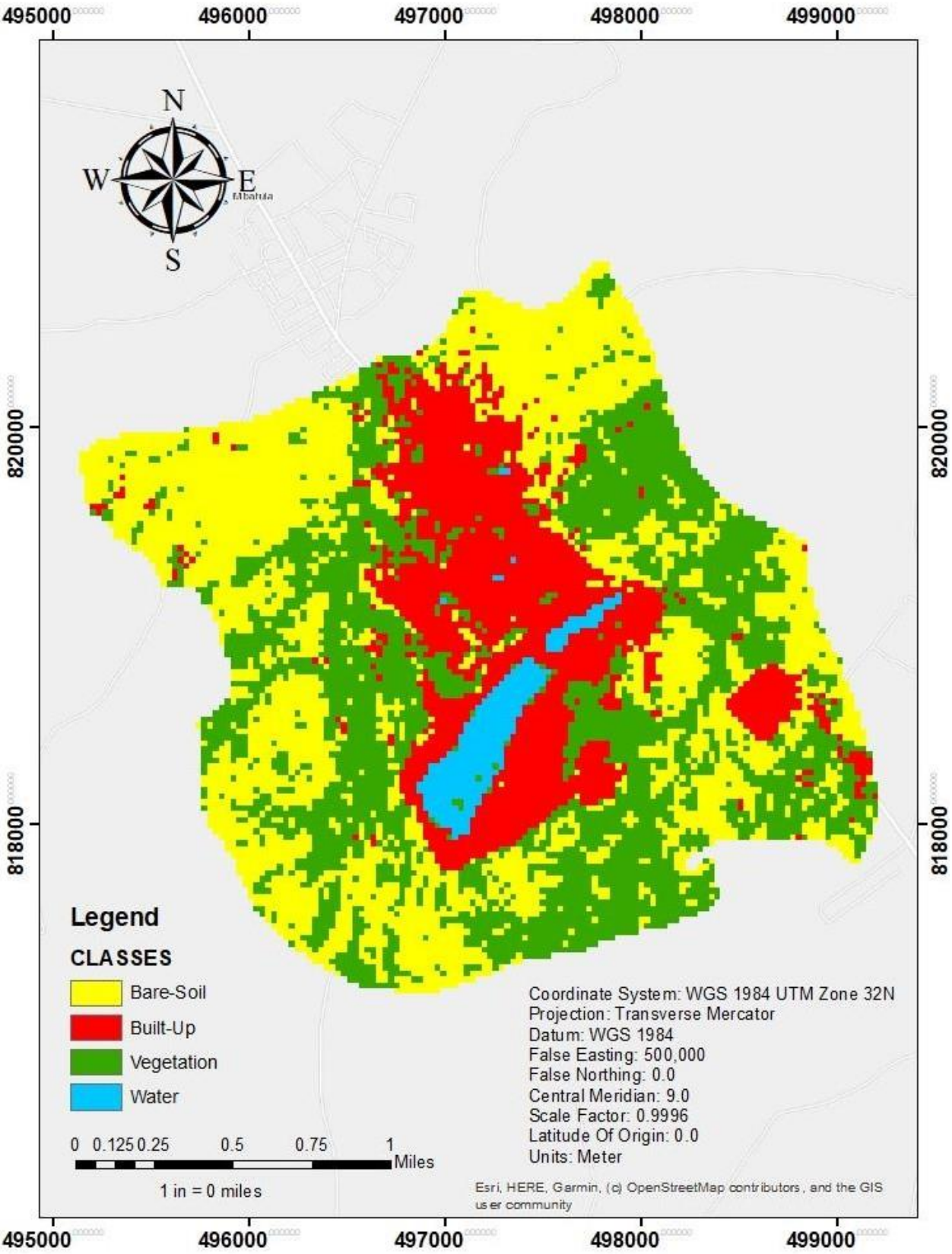

Figure 3: LULC map for 2019

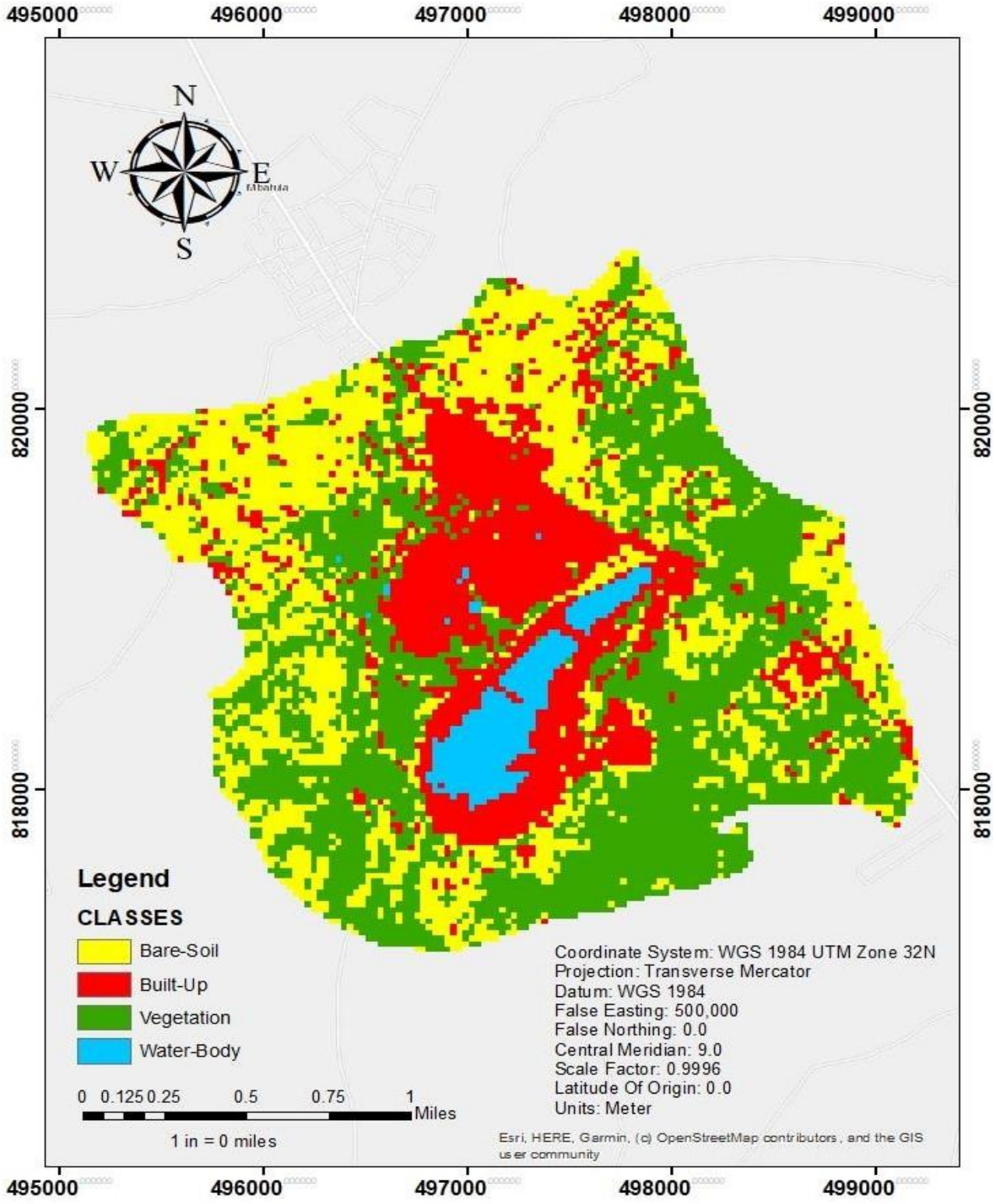

Figure 5: LULC map for 2024

3.3 Dynamics of Water Bodies and Bare Soil

Table 2 presented the summary of LULC analysis. Surface water exhibited a gradual increase from 0.18 km² in 2013 to 0.36 km² in 2024. This increase may reflect changes in hydrological conditions, improved sensor sensitivity, or the creation of artificial water bodies associated with urban development. Previous studies have similarly noted apparent increases in mapped water bodies in recent Landsat-based analyses, often linked to enhanced radiometric quality of newer sensors and improved water indices such as MNDWI (Hu et al., 2019).

Bare soil showed a contrasting trend, increasing sharply from 4.65 km² in 1986 to 5.28 km² in 2013, followed by a consistent decline to 3.07 km² in 2024. This pattern suggests that bare soil largely represents transitional land cover, which is eventually converted into built-up areas or vegetated surfaces. Such dynamics are characteristic of rapidly transforming landscapes and have been widely reported in LULC change studies focusing on urban growth corridors (Liping et al., 2018; Gondwe et al., 2021).

The results highlight urban expansion as the dominant driver of land transformation within the study area, with consequential impacts on vegetation, bare soil, and surface water dynamics. The findings reinforce the importance of integrating multi-temporal remote sensing data and machine learning techniques for monitoring long-term LULC changes and provide valuable insights for sustainable land use planning, environmental management, and policy formulation.

Table 2: Total area for each class in each year.

Year	Water (km²)	Built-Up (km²)	Vegetation (km²)	Bare Soil (km²)
1986	0	0.3332	4.1930	4.6467
2013	0.1754	1.3416	2.3748	5.2812
2019	0.2605	1.8847	3.3619	3.6658
2024	0.3615	2.0070	3.7393	3.0650

4.0 Conclusions

This study assessed long-term land use and land cover (LULC) dynamics within the study area over a 38-year period using multi-temporal Landsat imagery and a Random Forest (RF) machine learning approach implemented in the Google Earth Engine environment. By integrating spectral indices, NDVI, NDBI, MNDWI, and BSI, with Landsat surface reflectance data, the study achieved reliable discrimination of major land cover classes, including water bodies, built-up areas, vegetation, and bare soil.

The classification results demonstrated strong model performance, with overall accuracies exceeding 82% across all study years and Kappa coefficients indicating substantial to near-perfect agreement. These results confirm the robustness of the RF classifier and the suitability of Landsat data for multi-decadal LULC analysis, even in landscapes experiencing increasing heterogeneity due to urban growth.

The change detection analysis revealed pronounced expansion of built-up areas over time, reflecting sustained urbanization and infrastructure development. This expansion was accompanied by notable reductions in vegetation and increases in bare soil during earlier periods, followed by partial vegetation recovery and a decline in bare soil in more recent years. The gradual increase in surface water extent further highlights the dynamic nature of the landscape and potential changes in hydrological conditions or land management practices.

The findings underscore the value of integrating remote sensing, spectral indices, and machine learning techniques for monitoring spatio-temporal land transformations. The generated LULC maps and observed trends provide valuable information for urban planners, environmental managers, and policy-makers, supporting evidence-based decision-making aimed at sustainable land use planning, environmental conservation, and long-term resource management.

Acknowledgement
The authors acknowledge the support of Institute of Procurement, Environment and social Standards (IPESS).

References

Abass, K., Adanu, S. K., and Gyasi, R. M. (2018). Urban sprawl and land use/land-cover transition probabilities in peri-urban Kumasi, Ghana. *West African Journal of Applied Ecology*, 26, 118–132.

Cobbinah, P. B., Erdiaw-Kwasie, M. O., and Amoateng, P. (2015). Rethinking sustainable development within the framework of poverty and urbanisation in developing countries. *Environmental Development*, 13, 18–32.

Clerici, N., Cote-Navarro, F., Escobedo, F. J., Rubiano, K., and Villegas, J. C. (2019). Spatio-temporal and cumulative effects of land use land cover and climate change on ecosystem services in the Colombian Andes. *Science of the Total Environment*, 685, 1181–1192.

Dadson, I. Y. (2016). Land use and land cover change analysis along the coastal regions of Cape Coast and Sekondi. *Ghana Journal of Geography*, 8(2), 108–126.

Gondwe, J. F., Lin, S., and Munthali, R. M. (2021). Analysis of land use and land cover changes in urban areas using remote sensing: Case of Blantyre City. *Discrete Dynamics in Nature and Society*. https://doi.org/10.1155/2021/8011565

Hu, X. (2019). Land use and land cover change and environmental impacts. *Scientific Reports*, 9(1).

Kamwi, J. M., Chirwa, P. W., Manda, S. O., Graz, P. F., and Kätsch, C. (2015). Livelihoods, land use and land cover change in the Zambezi Region, Namibia. *Population and Environment*, 37(2), 207–230.

Kumasi, T. C., Obiri-Danso, K., and Ephraim, J. H. (2010). Community engagement in the sustainable management of rivers: Barekese catchment, Kumasi, Ghana. *Environment, Development and Sustainability*, 12(6), 927–943.

Liping, C., Yujun, S., and Saeed, S. (2018). Monitoring and predicting land use and land cover changes using remote sensing and GIS techniques: A case study of a hilly area, Jiangle, China. *PLOS ONE*, 13(7), e0200493.

Pettorelli, N., Vik, J. O., Mysterud, A., Gaillard, J. M., Tucker, C. J., and Stenseth, N. C. (2005). Using the satellite-derived NDVI to assess ecological responses to environmental change. *Trends in Ecology & Evolution*, 20(9), 503–510.

Verburg, P. H., Crossman, N., Ellis, E. C., Heinimann, A., Hostert, P., Mertz, O., and Zhen, L. (2015). Land system science and sustainable development of the earth system: A global land project perspective. *Anthropocene*, 12, 29–41.

Wulder, M. A., Masek, J. G., Cohen, W. B., Loveland, T. R., and Woodcock, C. E. (2012). Opening the archive: How free data has enabled the science and monitoring promise of Landsat. *Remote Sensing of Environment*, 122, 2–10.

Xu, H. (2006). Modification of normalized difference water index (NDWI) to enhance open water features in remotely sensed imagery. *International Journal of Remote Sensing*, 27(14), 3025–3033.

Cite this article as:

Dzever L.F, Shomkegh S.A. and Ugbaa M.S (2025). Effects of Limestone Mining Activities on Land Use and Land Cover Change Around Dangote Cement Factory, Gboko, Benue State. *Nigerian Journal of Environmental Sciences and Technology*, 9(2), pp. 181-195. https://doi.org/10.36263/nijest.2025.02.64